



Self-supported hierarchical crystalline carbon nitride arrays with triazine-heptazine heterojunctions for highly efficient photoredox catalysis

Zongzhao Sun^a, Haozhe Dong^b, Qi Yuan^d, Yueyang Tan^a, Wu Wang^c, Yabin Jiang^a, Jianyong Wan^a, Jiangwei Wen^b, Jianjing Yang^{b,*}, Jiaqing He^c, Tao Cheng^d, Limin Huang^{a,e,*}

^a Department of Chemistry, Southern University of Science and Technology, Shenzhen, Guangdong 518055, PR China

^b Institute of Medicine and Materials Applied Technologies, College of Chemistry and Chemical Engineering, Qufu Normal University, Qufu, Shandong 273165, PR China

^c Department of Physics, Southern University of Science and Technology, Shenzhen, Guangdong 518055, PR China

^d Institute of Functional Nano & Soft Materials (FUNSOM), Soochow University, Suzhou, Jiangsu 215123, PR China

^e Guangdong-Hong Kong-Macao Joint Laboratory for Photonic-Thermal-Electrical Energy Materials and Devices, Southern University of Science and Technology, Shenzhen 518055, PR China.

ARTICLE INFO

Keywords:

High crystallinity
Carbon nitride array
Photocatalysis
Water splitting
Aromatic hydrocarbons oxidation

ABSTRACT

Self-supported hierarchical crystalline carbon nitride arrays (MA-rod array), which show the excellent properties of photocatalytic hydrogen evolution and oxidative organic synthesis, were synthesized by molten salt-assisted pyrolysis of rod-like supramolecular precursors from the hydrolysis of melamine. On the nanoscale, the highly crystalline MA-rod array has an omasum-like architecture with combined advantages of rapid electrolyte diffusion, efficient gas evolution, fast electronic transmission, and lower interface resistance. At the molecular level, the triazine-heptazine heterojunctions remarkably improve charge carrier transfer and separation. In the tests of photoredox catalysis, the MA-rod array exhibited 51-fold higher hydrogen production rate ($11720 \mu\text{mol h}^{-1} \text{ g}_{\text{cat}}^{-1}$) than the reference with a high apparent quantum yield (AQY) of 60% at 420 nm. Furthermore, the oxidation of aromatic hydrocarbons to aldehydes or ketones can be obtained under single wavelength (460 nm) irradiation with milligram yields (e.g., the isolated yield of benzaldehyde is 34.5 mg with the conversion rate of $1805.6 \mu\text{mol h}^{-1} \text{ g}_{\text{cat}}^{-1}$), surpassing other photocatalysts so far.

1. Introduction

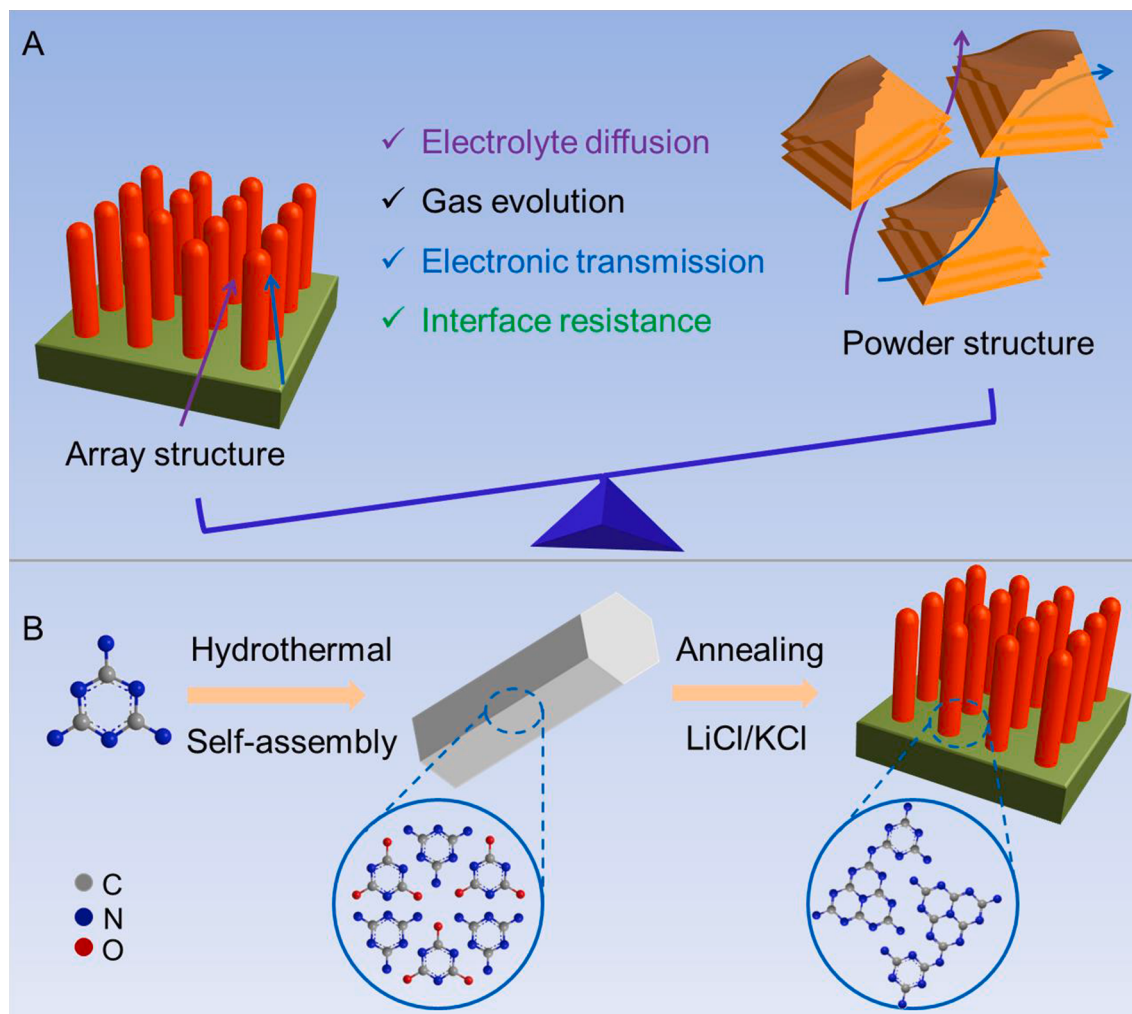
Solar energy conversion into chemical energy is widely considered as a promising clean energy technology.^[1–3] For instance, hydrogen production via water splitting driven by a photocatalyst can be expected to be a popular candidate to substitute fossil fuels.^[4–8] It is also attractive to synthesize high value-added products by selective photocatalytic organic transformation, especially the synthesis of aldehydes or ketones by selective oxidation of hydrocarbons.^[9–11] An efficient photocatalyst with a matched bandgap, stable molecular structure, and rapid charge carriers dynamics is necessary for realizing these wonderful visions. Graphitic carbon nitride (GCN) as a metal-free photocatalyst has been widely used in photocatalytic hydrogen evolution and selective oxidation of organic molecules since the first discovery in photocatalysis by Wang and coworkers.^[12] The facile synthesis, low-cost, environmental friendliness, excellent thermal and chemical stability, and appropriate band structure of GCN showcase its power in the field of

photocatalysis.^[13,14] However, the bulk GCN still suffers from low specific surface area, weak visible-light harvesting, and poor crystallinity. The insufficient photo-generated electron-hole pairs coupled with a high recombination rate and limited reactive sites greatly inhibit its applications.^[15–17] Now, a considerable amount of efforts, such as doping,^[18–20] crystal structure engineering,^[21–23] nanostructure designing^[24–27] and heterojunctions, etc^[28–30], have been made to optimize GCN-based photocatalysts in solar energy conversion and chemical synthesis.

Among these strategies, nanostructure designing, such as the creation of hierarchical nano/microstructures has been proven particularly effective with unique physical-chemical properties.^[31–35] Hard/soft templating is the common method to prepare GCN with specific morphology. Especially for those GCN with array structures, some hard templates such as ZnO, SiO₂,^[36–38] are usually used to support the networks for the fixed morphology. However, the subsequent template-removing procedure is time-consuming and not green because of the use

* Corresponding authors.

E-mail addresses: jjyang@whu.edu.cn (J. Yang), huanglm@sustech.edu.cn (L. Huang).



Scheme 1. A) The comparison of array structure and particle/sheet structure. B) The synthesis path of self-supported hierarchical crystalline GCN array.

of some hazardous reagents. Moreover, there is no report on self-supported carbon nitride arrays so far. Significantly, a supramolecular preorganization strategy can allow for the control of morphology at the molecular level. Many novel works used the cyanuric acid-melamine complex as a starting material to construct GCN with ordered and hollow structures.^[39] For example, Fu et al. fabricated two kinds of GCN-based nanostructure: ultrathin porous bundles and phosphorus-doped tubes for enhanced visible-light photocatalytic hydrogen evolution.^[40,41] Our group also constructed GCN tubes with porous coral-like architecture inside.^[24,42] In-situ electron microscopy revealed the evolution of cyanuric acid-melamine complex to the hollow structure from 3D insight and electron tomography first characterized the double-layer structure of the tube wall. We found that GCN prepared by these methods often has poor crystallinity and many structural defects, leading to low migration dynamics of charge carriers. Therefore, the improvement of crystallinity during pyrolyzing a supramolecular precursor is a promising strategy for further enhancing the photoredox activity. In addition, constructing heterojunctions contributes to forming a built-in electric field to promote the efficient separation of photogenerated electron-hole pairs.^[43] Especially for homologous ones, the effect can be further enhanced by the similar physico-chemical property,^[44] refer to the rutile and anatase phases of TiO₂.^[45] Fortunately, triazine-based poly(triazine imide) (PTI) and heptazine-based poly(heptazine imide) (PHI) have provided an available opportunity to fabricate triazine-heptazine heterojunctions for photocatalysis.^[46–48] Beyond those reported GCN-based heterojunctions, here, self-

supported hierarchical crystalline GCN-based arrays will elevate the performance to new heights, relying on the synergy of the unique morphology and heterojunctions.

The array structure has great advantages compared to the powder structure. The rapid electrolyte diffusion, efficient gas evolution, fast electronic transmission, and lower interface resistance guarantee more applicability of the array structure for photoredox catalysis. Studying self-supported arrays in heterocatalysis shows more scientific significance than most powder systems (**Scheme 1A**). Herein, we introduced a green method for producing self-supported crystalline GCN arrays through sequential molecule self-assembly followed by a molten salt-assisted polycondensation process (**Scheme 1B**). At the early stage, after a dissolution-recrystallization process, melamine underwent a hydrolysis reaction for the in-situ transformation to cyanuric acid. The self-assembly between them proceeded via hydrogen bonding to form hexagonal rod precursors. Then a mixture of LiCl/KCl was introduced to assist the calcination of precursors. After that, an omasum-like crystalline carbon nitride array (MA-rod array) with triazine-heptazine heterojunctions was obtained (**Scheme 1B**). As a liquid solvent, the molten salts could accelerate the polymerization process and further tailor the structure and properties of the co-polymers. The crystallinity, morphology and sub-unit heterojunctions synergistically endowed MA-rod array excellent ability of photoredox. In the test of hydrogen production under visible light irradiation, the as-synthesized sample exhibited high activity with an apparent quantum yield (AQY) of 60% at 420 nm. Especially, the aromatic C–H bond activation was realized with

high yields at the milligram level under 460 nm, which is an order of magnitude higher than the previous works.

2. Experimental section

2.1. Preparation of catalysts

Melamine-derived bulk carbon nitride (MA-CN): 1 g melamine was placed into a covered crucible and transferred to a horizontal tube furnace before heated to 550 °C with a ramp rate of 5 °C min⁻¹, and then held at that temperature for 4 h in a N₂ flow. After cooling to ambient temperature, the resulting solid was ground for subsequent use.

Melamine-derived carbon nitride tube (MA-CNT): 1 g melamine was first thoroughly dissolved in 70 mL deionized water at 80 °C. Then the solution was ultrasonicated in a cold water bath to make melamine recrystallized. After being transferred into a Teflon-lined stainless steel autoclave for a hydrothermal treatment at 200 °C for 12 h, the white rod-like products were obtained by filtration and drying at 60 °C. The following pyrolysis procedure was the same as the synthesis of MA-CN.

Melamine-derived poly(triazine imide) (MA-PTI): 0.50 g melamine, 0.9 g lithium chloride and 1.1 g potassium chloride were ground together in a mortar. Then the mixture was transferred into a glass tube with a cover. The tube was placed in a muffle and heated at 400 °C for 4 h with a ramp rate of 5 °C min⁻¹. After cooling down, the tube was evacuated and sealed. The sealed tube was heated at 550 °C for 12 h with a ramp rate of 5 °C min⁻¹. Finally, the cooled sample was isolated and washed with deionized water to remove the residual salts. The resulting MA-PTI was collected by centrifugation and drying at 60 °C.

Melamine-derived poly(heptazine imide) (MA-PHI): First, 2 g melamine was placed into a covered crucible and transferred to a horizontal tube furnace before heated at 550 °C for 4 h with a ramp rate of 5 °C min⁻¹. After cooling to ambient temperature, the resulting solid (melon) was ground for subsequent use. Second, 1 g melon and 2 g potassium thiocyanate were thoroughly ground in a mortar and transferred into a crucible in a tube furnace. The sample was heated in Ar-flow at 400 °C for 1 h with a ramp rate of 5 °C min⁻¹ and to 500 °C for 4 h with the same ramp rate. After cooling to room temperature, the solid was washed with deionized water to remove the residual salt. The resulting MA-PHI was obtained after centrifugation and drying at 60 °C.

Melamine-derived self-supported hierarchical crystalline carbon nitride array (MA-rod array): The rod-like precursor was obtained by following the procedure of MA-CNT. Subsequently, the precursor was thoroughly mixed with 1.8 g potassium chloride and 1.3 g lithium chloride. Then the mixture was transferred into a horizontal tube furnace and heated to 550 °C in a N₂ flow with a ramp rate of 5 °C min⁻¹, and held at that temperature for 4 h. After cooling to ambient temperature, the resulting solid was washed with deionized water to remove the residual salts. The resulting MA-rod array was obtained after centrifugation and drying at 60 °C.

2.2. Characterization

Transmission electron microscopy (TEM), STEM and EDS mapping were obtained from a Talos TEM operated at 200 kV. Electron energy loss spectroscopy (EELS) was conducted on a Titan ETEM G2. A Scanning Electronic Microscope (Merlin) was used to obtain SEM images at 3 kV and 5 kV. Powder X-ray diffraction (XRD) was performed on a Rigaku smartlab system operated at 45 kV and 200 mA using Ni-filtered Cu-K α radiation. The surface area analysis was carried out on a Micromeritics Model ASAP 2020 instrument at liquid nitrogen temperature based on N₂ adsorption-desorption isotherms. Solid-state ¹³C NMR spectra were measured on a Bruker Advance III 600 spectrometer. Fourier transform infrared (FT-IR) spectra were conducted on a Bruker VERTEX 70 spectrophotometer. Surface chemical analysis and valence band spectrum were recorded on a Kratos XSAM800 spectrometer with Al K X-rays radiation operated at 300 W. Diffuse reflection spectra were observed on

a Scan UV-vis spectrophotometer (PerkinElmer, Lambda 750S) in the range of 300–800 nm. The photoluminescence spectra were obtained using an Edinburgh spectrometer at an excitation wavelength 380 nm. The room temperature EPR spectra were collected on a Bruker EMXPlus-10/12-3.8 k spectrometer with a microwave frequency 9.8 GHz. The elemental composition results were characterized by an elemental analyzer (Elementar Vario EL cube). Thin-layer chromatography (TLC) employed glass 0.25 mm silica gel plates. Flash chromatography columns were packed with 200–300 mesh silica gel in petroleum (b.p. 60–90 °C). ¹H, ¹³C and ¹⁹F NMR data were recorded on a Bruker Advance III (500 MHz) spectrometer with tetramethylsilane as an internal standard. All chemical shifts (δ) are reported in ppm and coupling constants (J) in Hz. All chemical shifts are reported relative to tetramethylsilane and d-solvent peaks (77.00 ppm, chloroform), respectively.

2.3. Photoelectrochemical analysis

Transient photocurrent response and electrochemical impedance spectroscopy (EIS) were performed on a CHI 760 electrochemical workstation. A Pt wire, Ag/AgCl electrode and 0.1 mol L⁻¹ Na₂SO₄ aqueous solution were used as the counter electrode, reference electrode and supporting electrolyte, respectively. Firstly, 5 mg photocatalyst was dispersed in 1 mL ethanol with 100 μ L 0.05% wt Nafion solution. Then amounts of the suspension were transferred onto a glassy carbon electrode using a dispensing method. After drying, the working electrode was immersed in the Na₂SO₄ aqueous solution to perform the photocurrent experiment using a full automatic 10 W LED lamp. The frequency was set from 1 MHz to 0.01 Hz for the EIS tests.

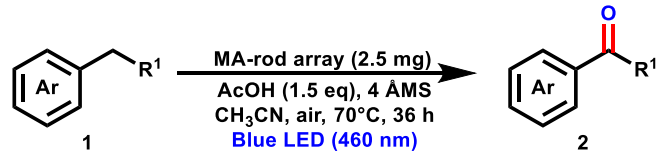
2.4. Photocatalytic hydrogen evolution

20 mg catalyst was first suspended in 40 mL aqueous solution. Then 10 mL triethanolamine as the sacrificial electron donor and 3% wt Pt as the co-catalyst was added. The suspension was thoroughly degassed under ultrasonication. A 300 W Xe lamp with a 420 nm filter was used to offer a light source. The photocatalytic H₂ yields were determined by an online gas chromatograph (SHIMADZU GC-2014C, TCD detector, Ar carrier gas, 5 Å molecular sieve column). The stability test was performed in 5 cycles under the standard condition for 25 h.

The average intensity of irradiation was measured on a Coherent Fieldax-T0 spectroradiometer for the wavelength-dependent apparent quantum yield (AQY) using the 420, 450, 500, 600 nm band-pass filter. And the AQY was estimated as follows:

$$\text{AQY} (\%) = \frac{2 * \text{number of evolved H}_2 \text{ molecules}}{\text{number of incident photons}}$$

2.5. Photocatalytic organic transformation

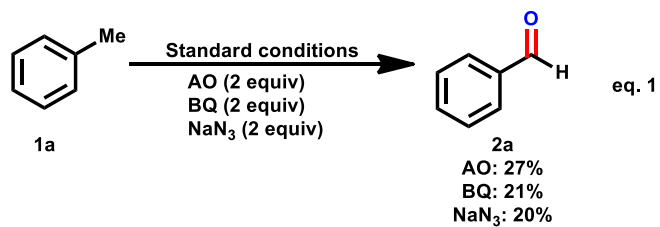


2.5 mg of MA-rod array, aromatic hydrocarbons 1 (0.25 mmol), AcOH (1.5 equiv), 40.0 mg 4 Å molecular sieves (MS) were first dispersed in 2.0 mL CH₃CN under air atmosphere. Then the mixture was stirred at 70 °C under blue light (460 nm) irradiation for 36 h. After the reaction was completed, the concentrated mixture was treated by flash column chromatography on silica gel (petroleum: dichloromethane = 10:1–50:1) to obtain corresponding naphthalene products 2.

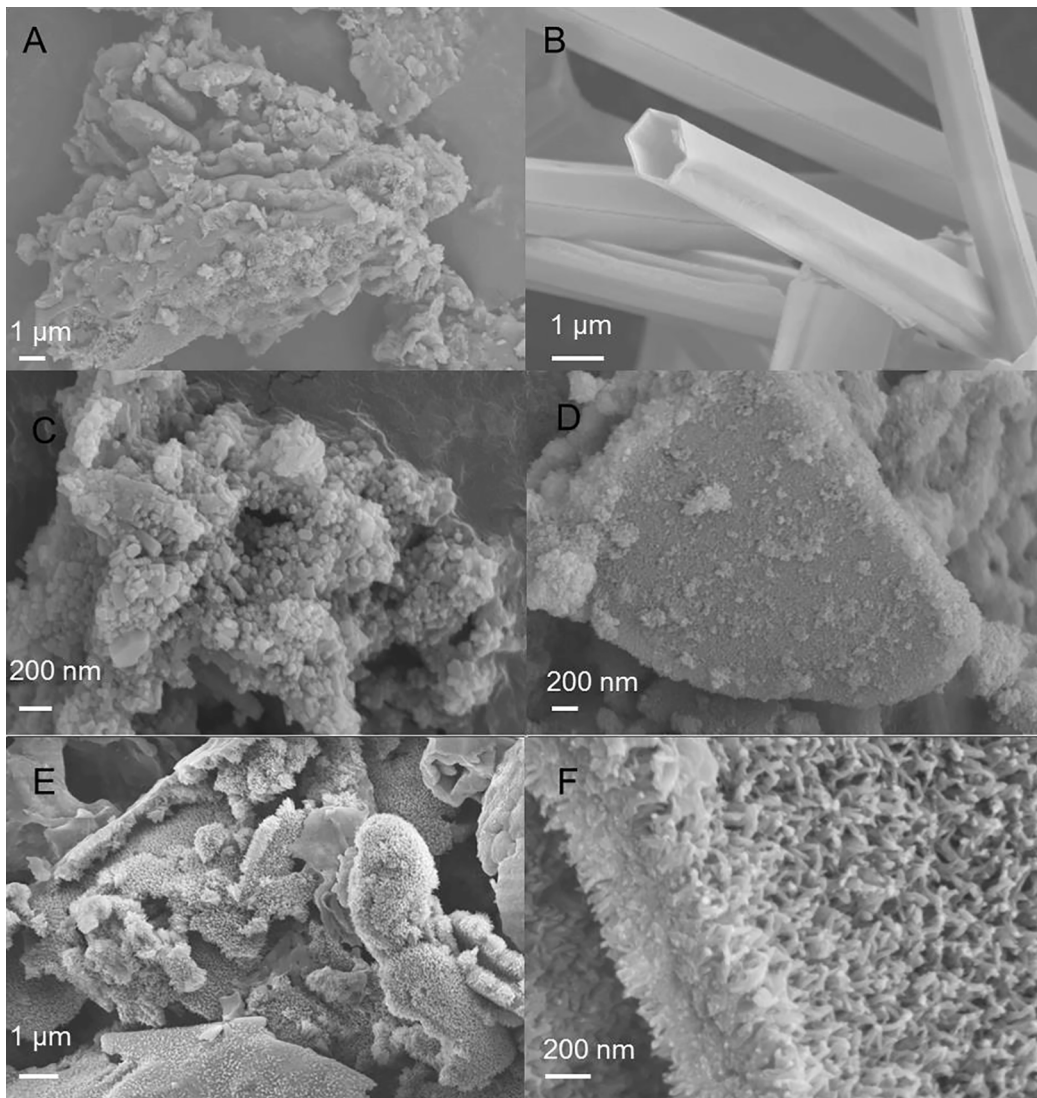
Table 1

Comparison of the five typical carbon nitride materials.

Materials	Morphology	Crystallinity	Sub-unit	Method
MA-CN	bulk/sheet	amorphous	heptazine	pyrolysis
MA-CNT	tubular	amorphous	heptazine	hydrothermal/ pyrolysis
MA-PTI	rod	highly crystalline	triazine	molten salt (LiCl/ KCl)
MA-PHI	particle	highly crystalline	heptazine	molten salt (KSCN)
MA-rod array	array	highly crystalline	triazine/ heptazine	hydrothermal/ LiCl/KCl

2.6. Preliminary mechanistic studies**2.6.1. Active species trapping experiments**

2.5 mg of MA-rod array, toluene **1a** (0.25 mmol), 4 Å MS (40.0 mg), AcOH (1.5 equiv), and two equivalent of ammonium oxalate (AO: hole scavenger), or benzoquinone (BQ: superoxide scavenger) or sodium azide (NaN_3 : singlet oxygen scavenger) were first dispersed in 2.0 mL CH_3CN under air atmosphere. Then the mixture was stirred at 70 °C under blue light (460 nm) irradiation for 36 h. After the end of the reaction, the concentrated mixture was treated by a flash column chromatography on silica gel (petroleum: dichloromethane = 50:1) to obtain products **2a** in 27%, 21% and 20% yield, respectively.

**Fig. 1.** SEM images of A) MA-CN, B) MA-CNT, C) MA-PTI, D) MA-PHI and E) MA-rod array with F) magnifying region.

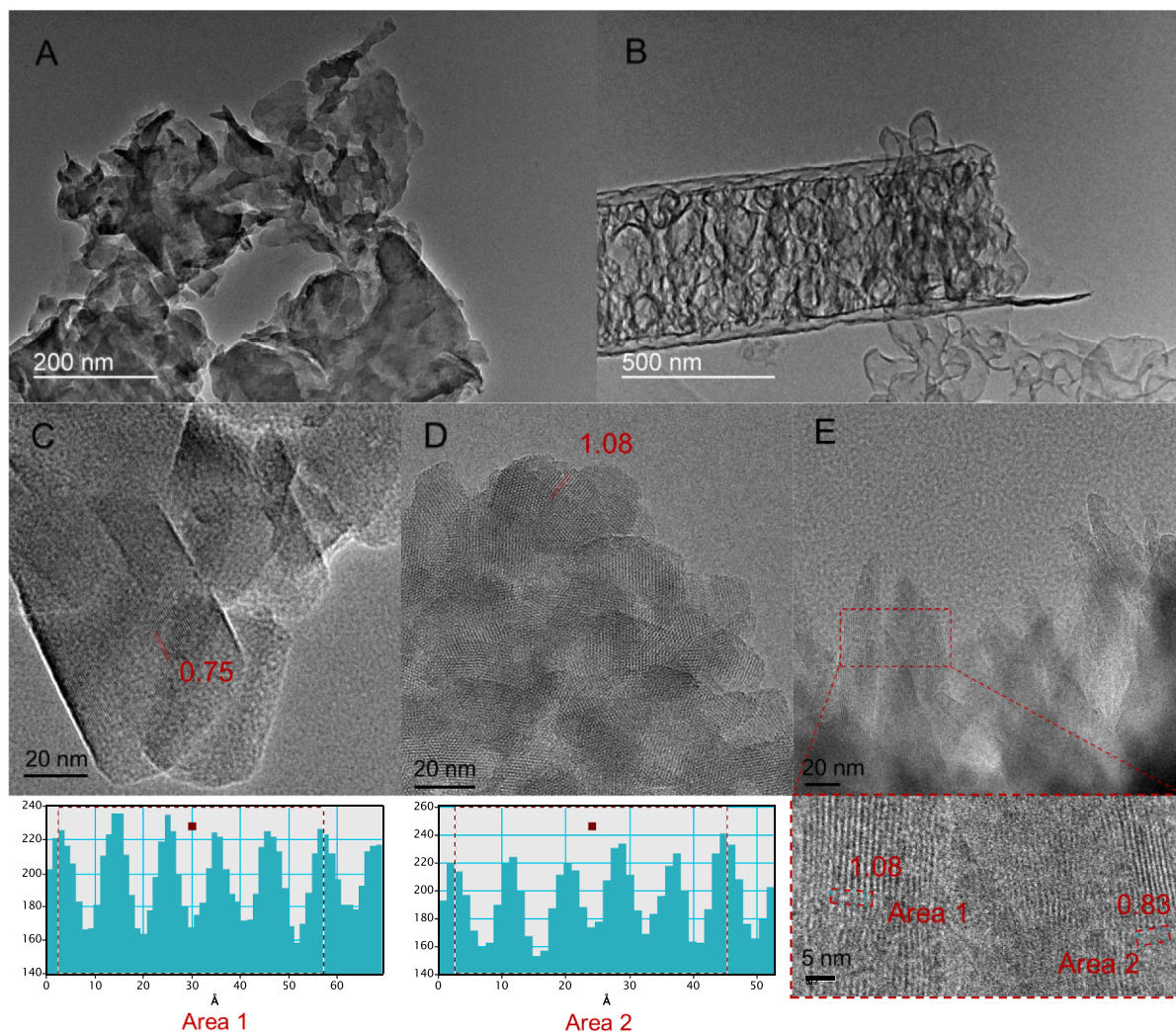
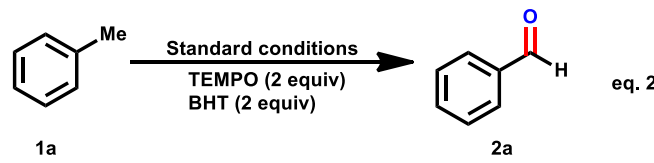


Fig. 2. TEM images of A) MA-CN, B) MA-CNT, C) MA-PTI, D) MA-PHI and E) MA-rod array with a selected magnifying area and the corresponding lattice distances in areas 1 and 2.

2.6.2. The reaction of **1a** with TEMPO or BHT under the standard conditions



Under the standard conditions, MA-rod array (2.5 mg), toluene **1a** (0.25 mmol), AcOH (1.5 equiv), 4 Å MS (40.0 mg), TEMPO or BHT (1.0 mmol) and CH₃CN (2.0 mL) were separately added. The mixture was then stirred at 70 °C under blue light (460 nm) irradiation for 36 h. After the reaction was completed, the information of product **2a** was undetected by a thin layer chromatography (TLC).

2.7. Computational methods

The quantum mechanics (QM) calculations were carried out using the VASP Software of version 5.4.4, with the Perdew, Burke, and Ernzerhof (PBE) flavor of density functional theory (DFT). The projector augmented wave (PAW) method was used to account for core-valence interactions. The kinetic energy cutoff for plane wave expansions was

set to 480 eV. The reciprocal space was sampled by the Γ -centered Monkhorst-Pack scheme with a grid of $3 \times 3 \times 1$ for structure optimization and $11 \times 11 \times 11$ for density of state (DOS) calculation. The vacuum layer is at least 10 Å above the surface. The convergence criteria are 1×10^{-7} eV energy differences for solving the electronic wave function. All geometries (atomic coordinates) were converged to within 1×10^{-2} eV Å⁻¹ for maximal components of forces. A post-stage vdW DFT-D3 method with Becke-Jonson damping was applied.

3. Results and discussion

3.1. Synthesis and characterization of the five carbon nitride materials

Using melamine as the only precursor, we prepared five typical carbon nitride materials, summarized in Table 1 in view of the morphology, crystallinity, sub-unit and synthesis method, including amorphous GCN: bulk GCN (MA-CN), tubular GCN (MA-CNT), and crystalline GCN: MA-PTI, MA-PHI and MA-rod array, to demonstrate the superiority of array structure in

photocatalysis. The scanning electron microscopy (SEM) images in Fig. 1 exhibit different morphologies. Fig. 1A shows large bulk structures for the reference MA-CN, which was synthesized by a traditional route. MA-CNT (Fig. 1B), the amorphous tubular CN obtained by supermolecular preorganization, shows hollow structures with a tube

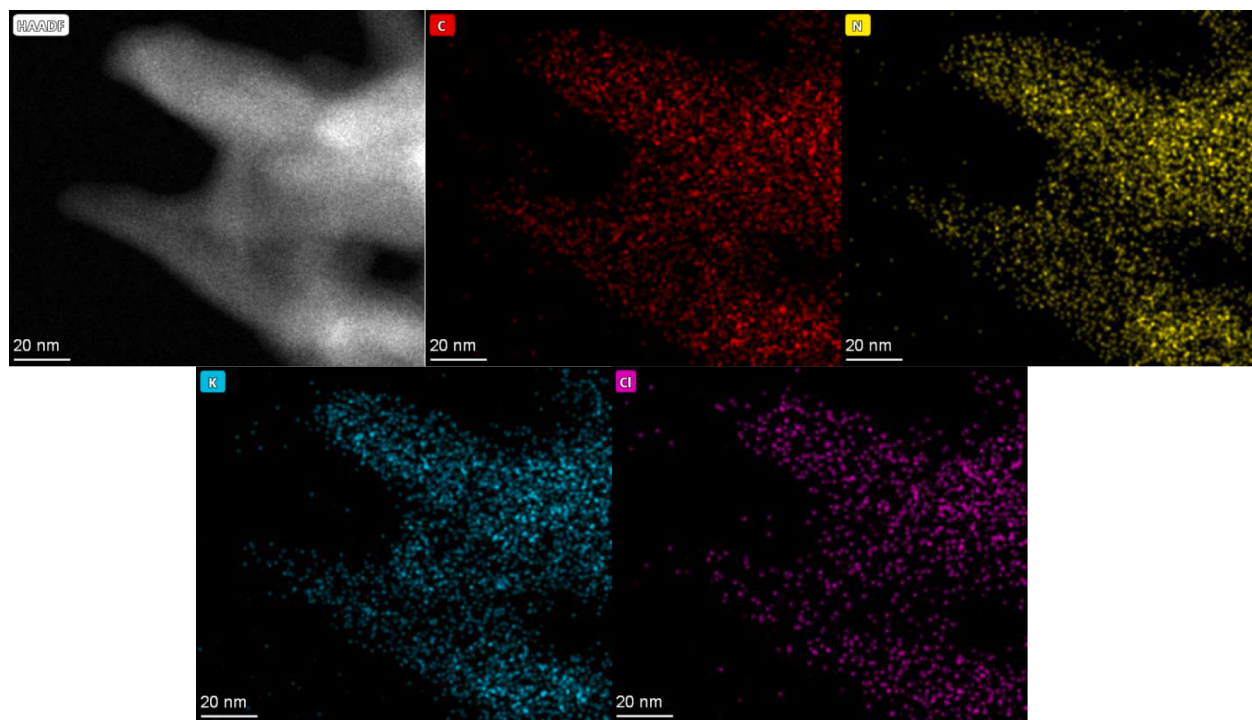


Fig. 3. HAADF-STEM image and EDS mapping of MA-rod array.

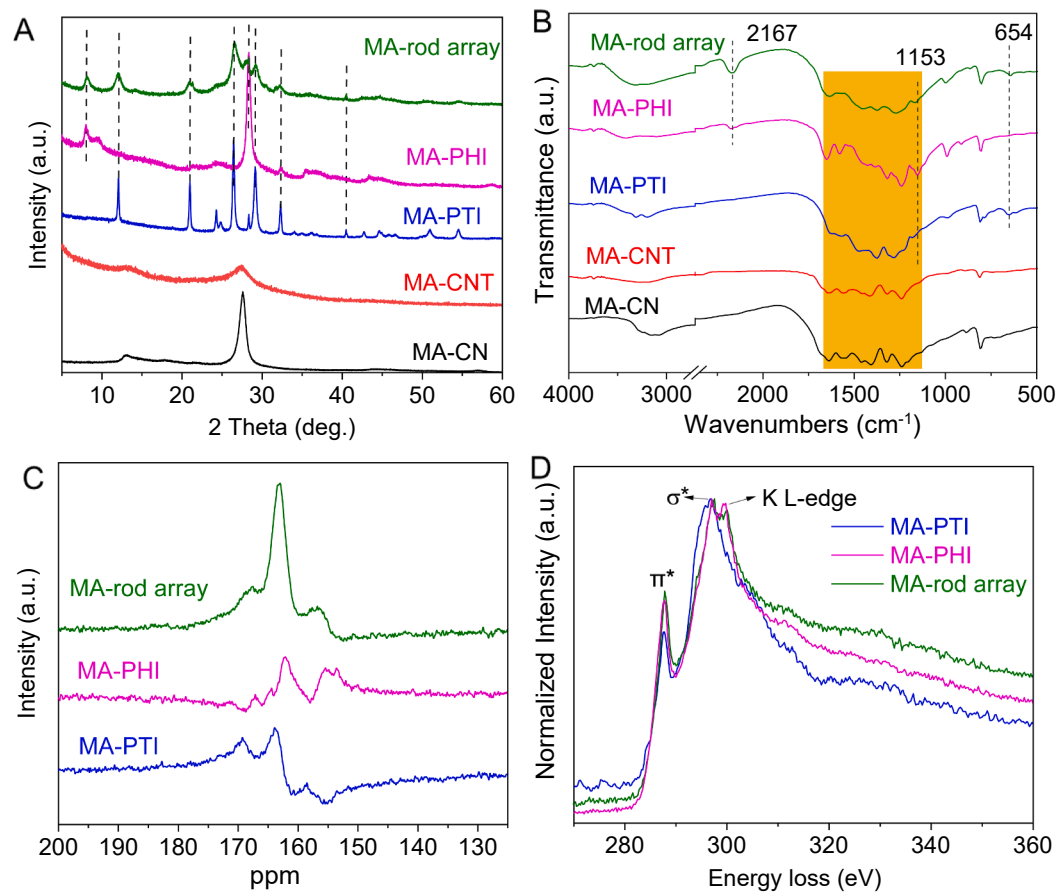


Fig. 4. A) XRD patterns and B) FT-IR spectra of MA-CN, MA-CNT, MA-PTI, MA-PHI and MA-rod array; C) ¹³C solid-state NMR spectra and D) EELS spectra near carbon K-edge of MA-PTI, MA-PHI and MA-rod array.

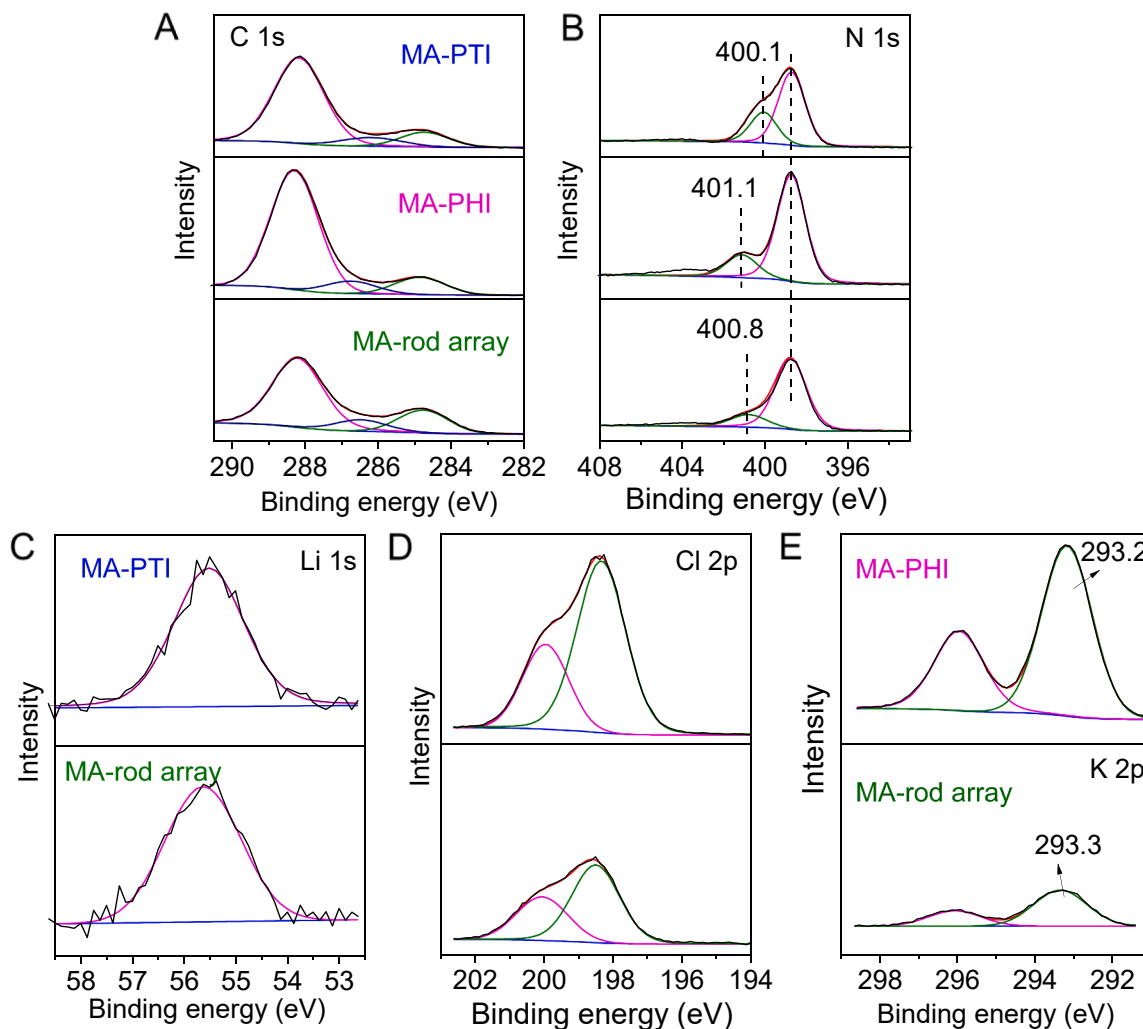


Fig. 5. XPS spectra of A) C 1 s and B) N 1 s of MA-PTI, MA-PHI and MA-rod array; The comparison of C) Li 1 s and D) Cl 2p in MA-PTI and MA-rod array; E) K 2p spectra in MA-PHI and MA-rod array.

diameter of approximately 1 μm . MA-PTI (Fig. 1C) prepared by molten salt (LiCl/KCl) with melamine displays regular rod-like structures with 40–50 nm in diameter. Conversely, MA-PHI synthesized by molten salt (KSCN) and melamine (Fig. 1D) looks like an agglomeration of many small particles. MA-rod array (Fig. 1E), obtained from the combination of supermolecular preorganization and molten salt (LiCl/KCl) synthesis, shows the hierarchical omasum-like architecture and lots of bristling rods (Fig. 1F) in the vertical direction with a diameter of approximately 20 nm. The addition of a eutectic mixture (LiCl/KCl) provides a highly confined environment and the liquidity accelerates the mass transfer during the reaction. The strong solvation and coordination effects modulate the route of carbon nitride polymerization, thus leading to the total collapse of the tube structure and the formation of the array structure.

The structures of the above materials can be further disclosed by the transmission electron microscopy (TEM) images in Fig. 2. The amorphous MA-CN (Fig. 2A) and MA-CNT (Fig. 2B) show the typical two-dimensional planar structure and tubular structure, respectively. Consistent with the SEM results, MA-PTI (Fig. 2C) has about the length to diameter ratio of 1:2 with the characteristic lattice fringe of 0.75 nm. In comparison, the small particles-aggregated MA-PHI (Fig. 2D) shows the characteristic lattice fringe of 1.08 nm. Fig. 2E shows the tentacles at the edge of MA-rod array with two kinds of lattice fringes: 1.08 nm (Area 1) and 0.83 nm (Area 2), corresponding to the feature of PHI and PTI,

respectively.

The slightly enlarged lattice fringe (0.83 nm) in the MA-rod array may be ascribed to the pulling effect of heptazine units and the insertion of K^+ induced lattice mismatch. High-angle annular dark-field scanning transmission electron microscopy (HAADF-STEM) and energy-dispersive X-ray spectroscopy (EDS) mappings in Fig. 3 provide the element distribution, where C, N, K, Cl exist uniformly along the tentacle-like morphology of MA-rod array. The element analysis in Table S1 shows the decreasing contents of both C and N in crystalline GCN. The C/N ratio (0.582) in MA-rod array lies between that of MA-PTI (0.5723) and MA-PHI (0.5979). With the increasing H content in MA-rod array, the formation of triazine-heptazine heterojunctions makes more terminal amino groups exposed. The X-ray photoelectron spectroscopy (XPS) surface elements scanning in Table S2 further verified the results of EDS mapping, where MA-rod array has the contents from both MA-PTI and MA-PHI.

X-ray diffraction (XRD) results in Fig. 4A revealed the phase structure of the five samples. The amorphous MA-CN and MA-CNT only have two characteristic peaks at 12.8° and 27.6°, corresponding to the in-plane arrangement and the interplanar stacking of triazine rings, respectively. The crystalline MA-rod array integrates the peaks of MA-PTI and MA-PHI, such as 12°, 21.0°, 26.6°, 29.2°, 32.3°, 40.5° (MA-PTI) and 8.0°, 28.3° (MA-PHI), among which the peaks 8.0° and 12° corresponding to the in-plane arrangement of sub-units match well with

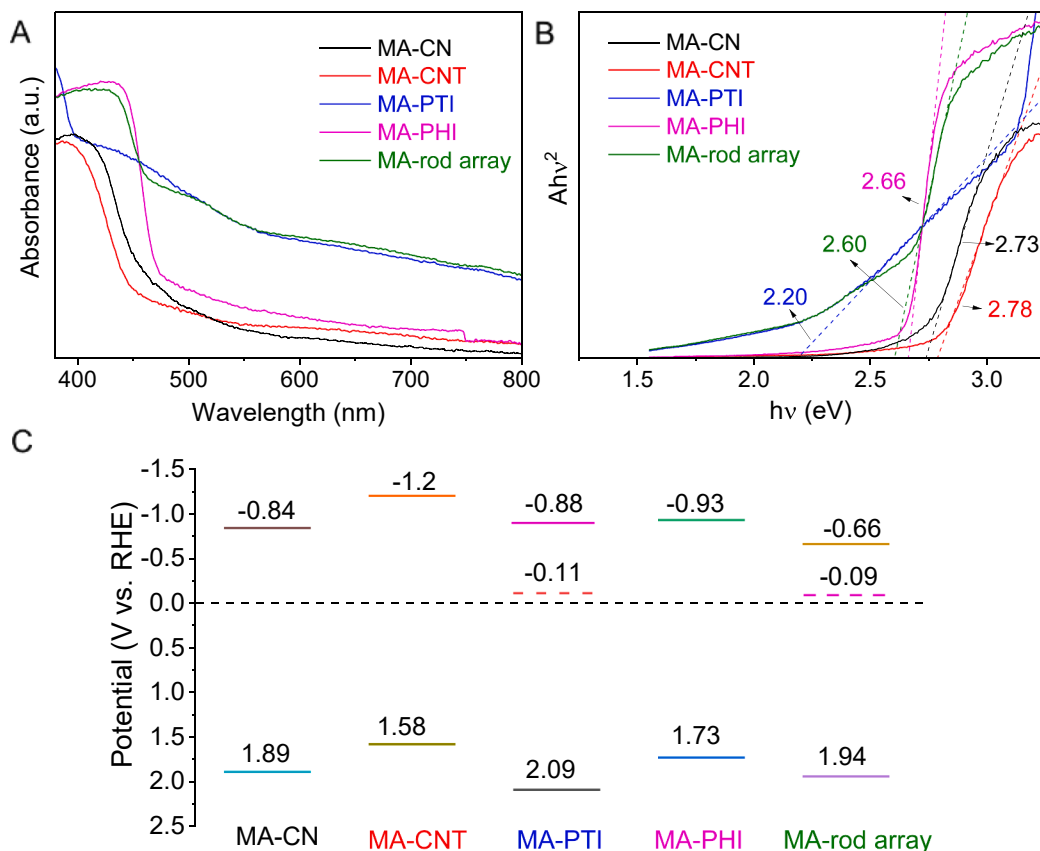


Fig. 6. A) UV-vis light absorption spectra and B) Plots of transformed Kubelka-Munk function versus photon energy; C) Corresponding diagrams for the band structures of MA-CN, MA-CNT, MA-PTI, MA-PHI and MA-rod array.

the lattice fringes in Fig. 2C and D. Moreover, Fourier transform infrared (FT-IR) spectra in Fig. 4B provide the structural information of all samples. MA-CN and MA-CNT exhibit the similar peaks at 1140–1640 cm⁻¹ (the yellow range) on behalf of the characteristic stretching vibration modes of C-N heterocycles following the typical GCN.^[49] The new peaks belonging to C-Cl at 654 cm⁻¹ in MA-PTI and 1153 cm⁻¹ implying the tricyclic “cyameluric” nucleus (C₆N₇), 2167 cm⁻¹ for terminal cyano groups in MA-PHI can also be found in the curve of MA-rod array. The enhanced intensity of MA-rod array in 3000–3500 cm⁻¹ representing N-H stretching vibration indicates the presence of more amino groups, which is consistent with the above element analysis results.

To further probe the local structures of MA-PTI, MA-PHI and MA-rod array, solid-state ¹³C nuclear magnetic resonance (NMR) spectra were recorded in Fig. 4C. MA-PTI shows three signals in the typical region. The signals at 158.5 and 164.0 ppm belong to C nuclei located next to the protonated triazine N atoms differentiated only by their Li⁺ environment, while C species adjacent to nonprotonated ring N atoms display the resonance at 169.3 ppm.^[50] For MA-PHI, the central C atom in the heptazine unit exhibits a chemical shift of 155.6 ppm. The signal at 162.1 ppm is attributed to a peripheral C atom next to a NH group (the protonated triazine N). The weak peak at 164.4 ppm arises from a C atom next to a deprotonated imide bridge. Additionally, the neighboring heptazine C atom is shifted downfield to 167.1 ppm due to the existence of cyano groups, which can likewise be observed in the FT-IR spectrum of MA-PHI. Interestingly, MA-rod array has combined NMR signals: 156.9, 163.1, 167.8 ppm compared with MA-PTI and MA-PHI. The slight chemical shifts may be derived from the interaction of different chemical environments of triazine and heptazine units. Furthermore, the electron energy-loss spectra (EELS) of MA-PTI, MA-PHI and MA-rod array were presented in Fig. 4D. All samples show the same π^* peaks

(287.79 eV) and σ^* peaks (296.75 eV) in C K-edges. The enhanced intensity of π^* peaks in MA-PHI and MA-rod array mean the enlarged conjugate degree. Unlike MA-PTI, MA-PHI and MA-rod array also have the evident K L-edges (ca. 299.75 eV), again confirming the existence of K⁺ between the polymeric chains.^[47] The N K-edges of all samples in Figure S1 have the same σ^* peaks (408.75 eV) for very similar chemical environments. But the π^* peak (399.75 eV) in MA-PHI and MA-rod array shifts toward lower energy than that in MA-PTI (400.25 eV), indicating that MA-PHI and MA-rod array have a higher π -electron density than MA-PTI. The small peak (401.25 eV) in MA-PTI can also be found in MA-rod array (400.54 eV) with a slightly low energy shift, suggesting MA-rod array and MA-PTI have a partially similar structure.

The chemical states of crystalline GCN samples characterized by XPS are shown in Fig. 5. All samples show the similar fitted C 1 s peaks at 284.8, 286.4 and 288.3 eV (Fig. 5A) referring to adventitious hydrocarbons, C-NH_x on the edges of sub-units and N-C = N in sub-units, respectively. Surprisingly in N 1 s spectra (Fig. 5B), the fitted peak at 400.1 eV in MA-PTI and 401.1 eV in MA-PHI representing tertiary nitrogen groups and the defective amino groups tend to be neutralized in MA-rod array (400.8 eV) since the formation of triazine-heptazine heterojunctions as the main peak at 398.7 eV corresponding to C-N = C is invariant. The difference of binding energy in MA-PTI and MA-PHI dominates the electron migration from heptazine units to triazine units in MA-rod array. Besides, MA-rod array has the same peaks of Li 1 s (Fig. 5C) and Cl 2p (Fig. 5D) as MA-PTI with only lower intensity. But the K 2p peak at 293.3 eV in MA-rod array (Fig. 5E) shifts to higher binding energy than that in MA-PHI (293.2 eV), indicating lower electron density around the units. It suggests that K⁺ ions may be involved in the electron transfer from heptazine to triazine units in MA-rod array.

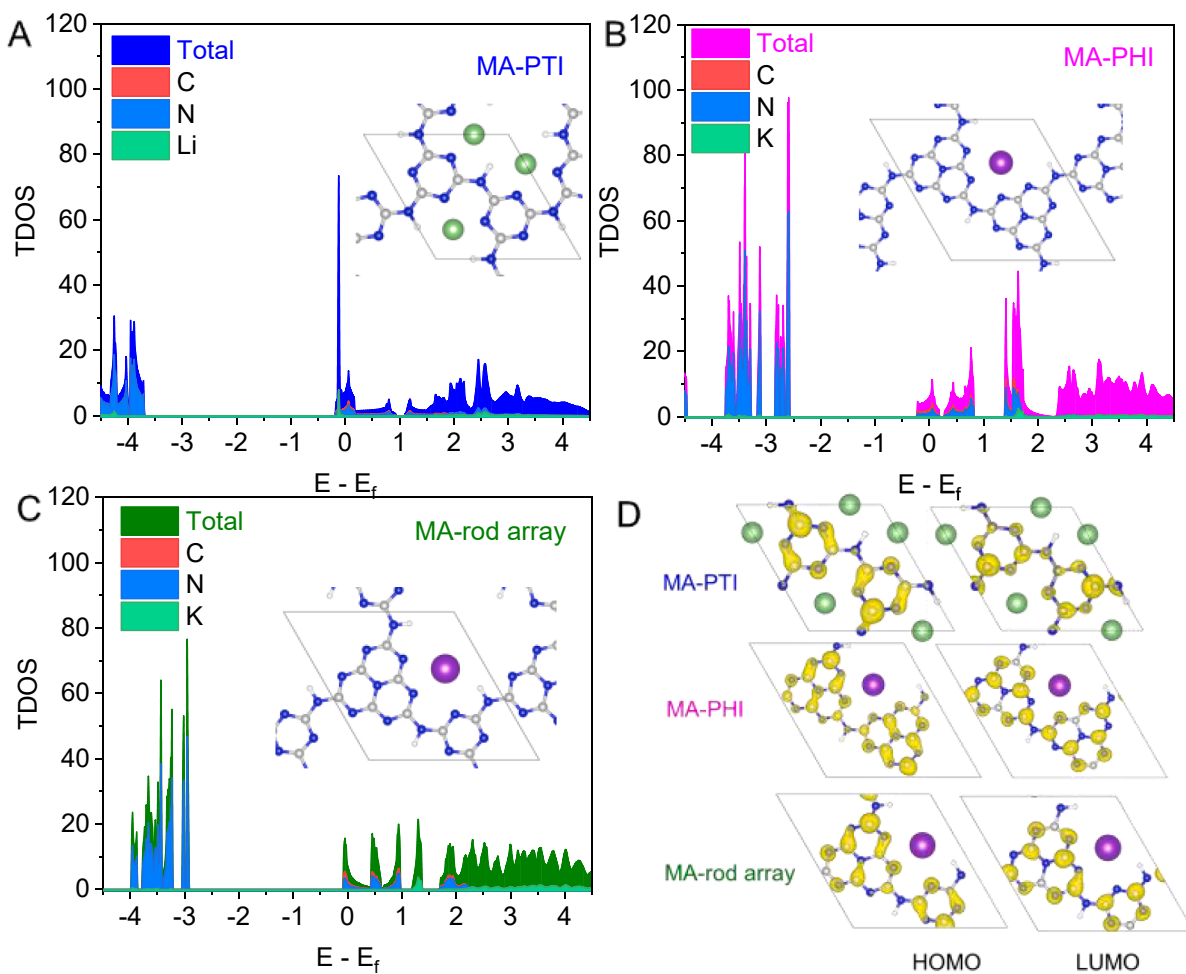


Fig. 7. Calculated density of states of A) MA-PTI, B) MA-PHI and C) MA-rod array with their inset models and D) the corresponding spatial charge distributions of HOMO and LUMO.

3.2. Electronic structures of the five carbon nitride materials

UV-vis light absorption spectra in Fig. 6A reflect the light-harvesting ability of samples. Crystalline MA-PTI, MA-PHI and MA-rod array show improved visible light absorption due to the fast migration dynamics of charge carriers. Moreover, MA-rod array inherits the feature of MA-PTI and MA-PHI. The absorption curve before 480 nm follows that of MA-PHI. Otherwise, the trends after 480 nm almost match well with that of MA-PTI. In other words, the heptazine and triazine units play their roles synergistically to improve the light absorption of MA-rod array. Additionally, both MA-PTI and MA-rod array have strong tail absorption (so-called Urbach tail) covering the whole visible-light region, which usually results from the existence of dopants/defects, leading to the formation of localized electronic states inside the original bandgap (known as midgap states). [24] Calculated by the Kubelka-Munk function versus photon energy, the bandgaps of the five samples are demonstrated in Fig. 6B and Figure S2. The amorphous MA-CN and tubular MA-CNT have relatively large bandgaps up to 2.73 eV and 2.78 eV, as well as MA-PTI (2.97 eV). In contrast, MA-PHI and MA-rod array have narrow bandgaps: 2.66, 2.60 eV, respectively. Besides, the midgaps of MA-PTI and MA-rod array can be determined at 2.20 eV and 2.03 eV, respectively. XPS valence band (VB) spectra were shown in Figure S3 to further investigate the band positions. With the tangent treatment, the VB maximums are calculated as 2.45 eV (MA-CN), 2.14 eV (MA-CNT), 2.65 eV (MA-PTI), 2.29 eV (MA-PHI) and 2.50 eV (MA-rod array). Converting by the formula E_{NHE}/V = φ + VB - 4.44 (where E_{NHE}: the

potential of normal hydrogen electrode; φ: the electron work function of the analyzer, usually 3.88 eV), [51] the real VB positions are confirmed to be 1.89, 1.58, 2.09, 1.73 and 1.94 eV for the five samples. Naturally, the band alignments are schematically described in Fig. 6C. Compared to bulk MA-CN, the conduction band (CB) of tubular MA-CNT is more negative than that of MA-CN for stronger reduction ability of photoelectrons in terms of thermodynamics, which was confirmed by our previous work. [24] Crystalline MA-PTI and MA-PHI have similar CB positions for thermodynamically driving photocatalytic reactions. The doping mid-CB positions of MA-PTI (-0.11 eV) and MA-rod array (-0.09 eV) are close to the zero potential, resulting in upward absorption tails in the visible light region for more solar energy injection. Besides, the more positive VB positions (2.09 eV and 1.94 eV) make it possible to realize the stronger oxidation of some organic molecules in MA-PTI and MA-rod array. Thus MA-rod array with triazine-heptazine heterojunctions integrates the advantages of MA-PTI and MA-PHI for potential photoredox catalysis.

The density functional theory (DFT) calculations were employed to investigate the contribution of electronic configuration in MA-PTI, MA-PHI, and MA-rod array. According to previous studies, the monolayer models were chosen (insert in Fig. 7A, B, and C) to represent the experimental analog because the simulation of the whole stacking patterns of crystalline GCN is computationally too expensive to be affordable. MA-rod array exhibits a higher intensity of electron densities of states (DOS) at the triazine-heptazine hetero-interface, particularly close to edges of CB than MA-PTI, which is similar to MA-PHI. It indicates that

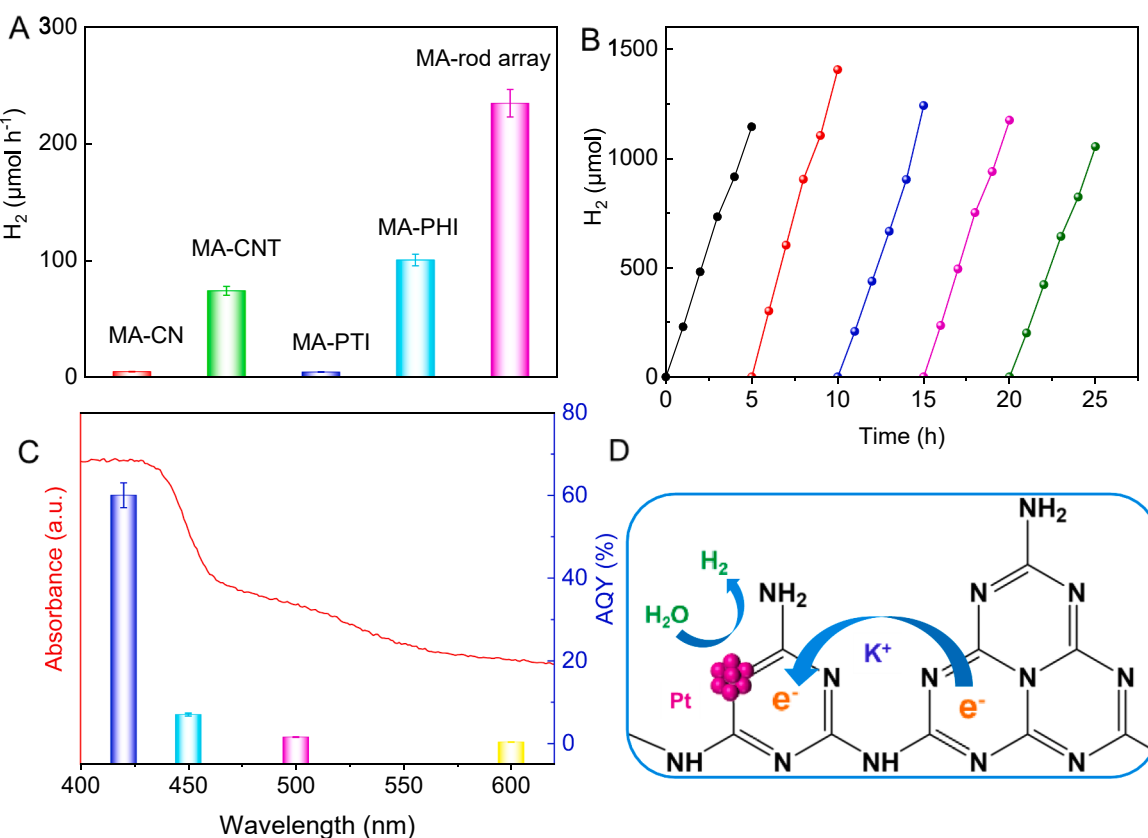


Fig. 8. A) The comparison of photocatalytic hydrogen evolution of the five samples, B) The cycling stability test of hydrogen evolution rate and C) wavelength-dependent apparent quantum yield of MA-rod array. D) Schematic of the proposed photo-electron transfer path in the framework of MA-rod array.

the heptazine units contribute to the increasing of electron density in CB. Fig. 7D shows the calculated electron density of the highest occupied molecular orbital (HOMO) and lowest unoccupied molecular orbital (LUMO) of MA-PTI, MA-PHI, and MA-rod array. The uniform distributions in MA-PTI and MA-PHI are ascribed to the high symmetry of the planar structure without any disturbance. In contrast, the electron density at the hetero-interface of the MA-rod array is inhomogenous, which can accelerate the rate of electronic disturbance for the directed migration. Such inhomogeneous distribution is potentially beneficial for photocatalytic activity.

3.3. Photocatalytic hydrogen evolution of the five carbon nitride materials

The hydrogen evolution rates of the five samples were measured in Fig. 8A with 3% wt Pt as a co-catalyst and 10 mL triethanolamine as the sacrificial electron donor. The bulk MA-CN shows a low activity of 230 $\mu\text{mol h}^{-1}$ g_{cat}⁻¹. By changing the morphology, tubular MA-CNT has an improved activity of 3690 $\mu\text{mol h}^{-1}$ g_{cat}⁻¹. But the crystalline MA-PTI displays a poor activity of 215 $\mu\text{mol h}^{-1}$ g_{cat}⁻¹, probably due to the insufficient reducing capacity in terms of the lower doping CB position (-0.11 eV) and excessive defects induced recombination of electrons and holes. Conversely, MA-PHI with a higher CB position (-0.93 eV) obtains a reasonable hydrogen production of 5005 $\mu\text{mol h}^{-1}$ g_{cat}⁻¹. MA-rod array has, as expected, the optimal activity of 11720 $\mu\text{mol h}^{-1}$ g_{cat}⁻¹ for 51 times higher than MA-CN. Moreover, this hierarchical array structure-based photocatalytic system undergoes a stable cyclic utilization for 25 h with inconspicuous attenuation (Fig. 8B). The XRD and TEM results in Figure S4 showed that the crystal structure and array architecture were well maintained after the reaction, showing the robust chemical stability of MA-rod array. The wavelength-dependent AQY in Fig. 8C conforms well with the variation trend of the UV-vis spectrum.

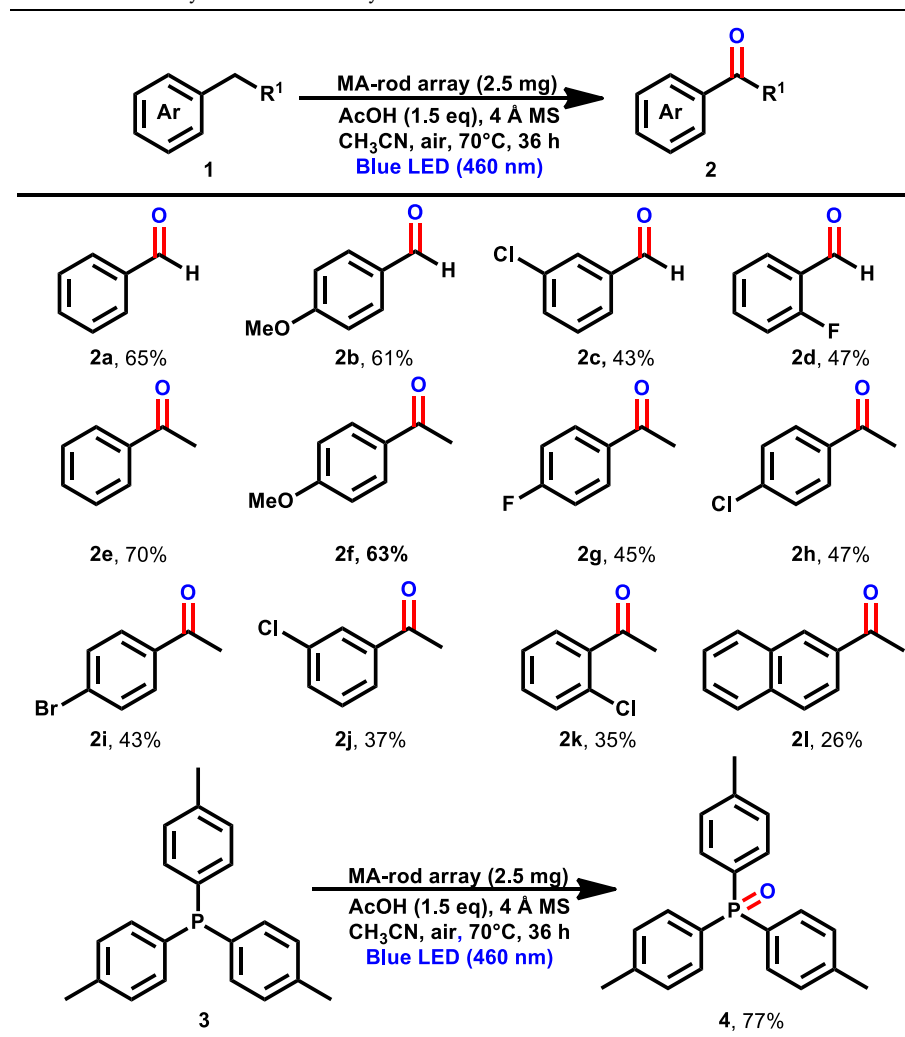
Excitingly, a relatively high value of 60.0% at 420 nm is obtained for efficient solar-to-energy conversion, surpassing most reports on GCN-based photocatalysts in Table S3.

3.4. Selective photocatalytic organic transformation over MA-rod array

The excellent photoredox activity of MA-rod array was further evaluated by the oxidation of aromatic C-H bonds, showing the great potential application in organic synthesis, including pharmaceutical and biologically active compounds, fine chemicals and organic transformations. Various substituted aromatic hydrocarbons were selected to conduct oxidative reactions with MA-rod array under optimized conditions. Table 2 shows that hydrocarbons **1** are transformed to aldehydes or ketones **2** directly by MA-rod array with satisfying yields at the milligram level under 460 nm irradiation, demonstrating its superior practicability. Taking toluene as an example, after one cycle of reaction, the isolated yield of benzaldehyde (**2a**) is up to 34.5 mg with the conversion rate of 1805.6 $\mu\text{mol h}^{-1}$ g_{cat}⁻¹. To the best of our knowledge, the performance is superior to the most reported GCN-based photocatalysts under the single wavelength, even exceeding some inorganic catalysts, hybrid catalysts and metal-organic frameworks (MOFs) in Table S4. The effects of various substitutions on the oxidative processes are also investigated.

Electron-donating groups such as methyl (Table 2, 2e), methoxyl (Table 2, 2b, 2f) contribute to higher conversion rates than the electron-withdrawing groups such as Cl (Table 2, 2c, 2h, 2j, 2k), Br (Table 2, 2i) or F (Table 2, 2d, 2g). To our delight, the desired product **2** **1** can be obtained with a yield of 26% when 2-ethylnaphthalene was performed in the present protocol. In addition, beyond the oxidation of aromatic C-H bonds, the oxidation of some aromatic heteroatoms can also be achieved. Under the same conditions, compound **3** can be transformed

Table 2
Oxidative aromatic hydrocarbons to aldehydes or ketones^{a,b}.



^a Standard conditions: 1 (0.25 mmol), MA-rod array (2.5 mg), AcOH (1.5 equiv), 4 Å MS (40.0 mg), CH₃CN (2.0 mL), 70 °C, Blue LED (460 nm), air, 36 h.

^b Isolated yield.

to compound 4 with a high isolated yield (77%, 61.6 mg), showing wide general applicability.

The active species trapping experiments were conducted to explore the oxidative mechanism of aromatic hydrocarbons forming aldehydes or ketones over MA-rod array. Ammonium oxalate (AO: hole scavenger), benzoquinone (BQ: superoxide scavenger) and sodium azide (Na₃N: singlet oxygen scavenger) were selected to illuminate the contribution of different active species to the reaction under the standard conditions (eq. 1). The conversion rate was drastically decreased after adding BQ and Na₃N (supporting information, 21% and 20%), and the transformation was also suppressed to some extent by AO (supporting information, 27%). Thus, the superoxide radical and singlet oxygen are determined as the major reactive species for the oxidation of aromatic hydrocarbons, and the hole also promotes the proceeding of this reaction. Moreover, the addition of free radical inhibitors (supporting information, TEMPO or BHT) in the reaction can significantly reduce the yield of the reaction, indicating that free radical intermediates are involved in the reaction (eq. 2). It is worth noting that this oxidation process undergoes a two-electron pathway, which matches well with the hydrogen production. Thus, the cascade reaction of simultaneous reduction and oxidation is expected to be achieved after the subsequent conditional optimization for greater significance.

3.5. The enhanced mechanism analysis

Photoluminescence spectra are shown in Fig. 9A to understand the enhanced mechanism. The crystalline samples (MA-PTI, MA-PHI, and MA-rod array) show the low intensity, indicating the suppressed electron-hole recombination, benefitting from the fast migration dynamics of charge carriers in the ordered crystalline phases. The existence of triazine-heptazine heterojunctions in MA-rod array further accelerates the effect by forming a donor-acceptor system. The generated intramolecular charge transfer has been proved to be a significant factor in determining the photocatalytic activity.[52–55] The efficient separation of charge carriers can be further confirmed by the photoelectrochemical tests in Fig. 9B and C. The periodic photocurrent measurement of the five samples exhibits rapid on/off responses to the visible light illumination. Significantly, MA-rod array shows an approximately five-fold increase of photocurrent density compared to MA-CN and MA-PTI, suggesting more photo-electrons injection. Moreover, the semicircular EIS Nyquist plot of MA-rod array in Fig. 9C displays a minimum radius for the lowest electron transfer resistance.

Thus, these photoelectrochemical measurements fully illustrate that the mobility of the photogenerated carriers is highly promoted. Especially, the array structure provides a favorable platform for electronic transmission and interface resistance, as mentioned in Scheme 1A. The

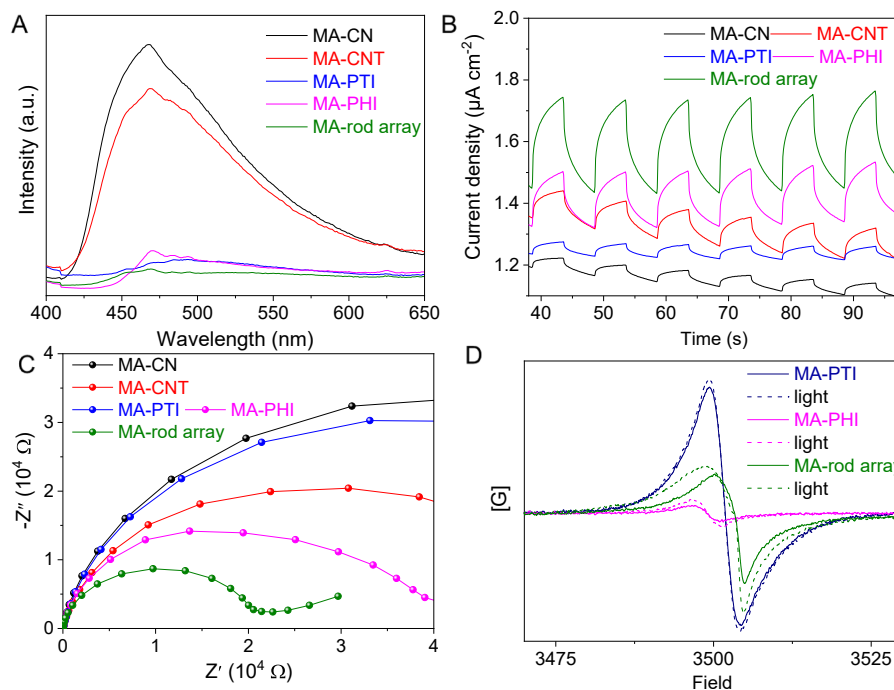


Fig. 9. A) Photoluminescence spectra, B) the periodic on/off photocurrent measurements and C) electrochemical impedance spectroscopy of the five samples under visible light irradiation. D) The room temperature electron paramagnetic resonance of MA-PTI, MA-PHI and MA-rod array.

room temperature electron paramagnetic resonance (EPR) in Fig. 9D revealed the electron delocalization. MA-PHI, MA-rod array, and MA-PTI have signals that increase sequentially for the intrinsic unpaired electron density. But MA-rod array presents an apparent rise (the green dotted line) compared to MA-PTI and MA-PHI after the light activation. Here more extra free radicals or unpaired electrons can easily stimulate catalytic reactions. Besides, the low specific surface area of MA-rod array in Figure S5 suggests that the enhanced activity mainly originates from the improvement of migration dynamics of charge carriers. Even so, there is still a lot of room for improvement in hydrogen evolution by optimizing the selection of GCN precursors with higher surface area and more exposed active sites. Based on the above characterization results, the proposed electron transfer process in MA-rod array with triazine-heptazine heterojunctions is demonstrated in Fig. 8D. The staggered bandgap in the heterojunction drives the electron transfer from heptazine units to triazine units. In the meantime, the potassium ion can act as a temporary bridge for the rapid electron migration and irreversible charge separation.

The remarkable improvement of the photocatalytic performance of MA-rod array results from integrated optimization of the morphology and electronic structure: First, the unique array configuration endows the MA-rod array with considerable superiorities for photoredox reactions, such as rapid electrolyte diffusion, efficient gas evolution, fast electronic transmission, and lower interface resistance as described in Scheme 1A. Besides, the high crystallinity of MA-rod array can significantly improve the mobility of charge carriers along the in-plane direction. The inserted ions (Li, K) also increase the transition chance of electrons between the layers. Second, the built-in electric field induced by triazine-heptazine heterojunctions can promote the separation of photogenerated electron-holes. Finally, the narrow bandgap enables MA-rod array to absorb more visible light, generating sufficient electrons and holes for photoredox catalysis.

4. Conclusion

A new strategy has been put forward for template-free fabrication of self-supported highly crystalline graphitic carbon nitride architecture

(MA-rod array) via sequential molecule self-assembly and molten salt-assisted polycondensation process. The MA-rod array with triazine-heptazine heterojunctions exhibits superior photocatalytic activity and stability for photocatalytic hydrogen production and aromatic hydrocarbons oxidation to form aldehydes or ketones under visible light or single wavelength irradiation with a high AQY (60.0%) and milligram yields, respectively. The unprecedented performance benefits from the synergic advantages of the array architecture and electronic structure for rapid electrolyte diffusion, efficient gas evolution, fast electronic transmission, low interface resistance, and remarkably improved charge carrier transfer and separation. This work paves the way for the morphology design of hierarchical crystalline GCN-based materials with excellent optical and electrical properties for versatile photo-involved catalysis and synthesis applications.

Declaration of Competing Interest

The authors declare that they have no known competing financial interests or personal relationships that could have appeared to influence the work reported in this paper.

Acknowledgements

This work was financially supported by Guangdong Provincial Key Laboratory of Energy Materials for Electric Power (2018B030322001), Guangdong Provincial Key Laboratory of Catalysis (2020B121201002), Shenzhen Clean Energy Research Institute (CERI-KY-2019-003), the Natural Science Foundation of Shandong Province (No. ZR2020QB130), the National Natural Science Foundation of China (Grant No. 11934007, 11874194, 51632005), the leading talents of Guangdong Province Program (Grant No. 00201517), the Science and Technology Innovation Committee Foundation of Shenzhen (Grant No. KQTD2016022619565991, JCYJ20200109141205978 and ZDSYS20141118160434515), and High level of special funds (G02206302). This work was also supported by the Pico Center at SUSTech that receives support from Presidential fund and Development and Reform Commission of Shenzhen Municipality.

Appendix A. Supplementary data

Supplementary data to this article can be found online at <https://doi.org/10.1016/j.cej.2022.134865>.

References

- [1] D. Kong, Y. Zheng, M. Kobielsz, Y. Wang, Z. Bai, W. Macyk, X. Wang, J. Tang, Recent advances in visible light-driven water oxidation and reduction in suspension systems, *Mater. Today* 21 (8) (2018) 897–924.
- [2] P. Zhang, X.W.(. Lou, Design of Heterostructured Hollow Photocatalysts for Solar-to-Chemical Energy Conversion, *Adv. Mater.* 31 (29) (2019) 1900281, <https://doi.org/10.1002/adma.v31.2910.1002/adma.201900281>.
- [3] T. Banerjee, F. Podjaski, J. Kröger, B.P. Biswal, B.V. Lotsch, Polymer photocatalysts for solar-to-chemical energy conversion, *Nat. Rev. Mater.* 6 (2) (2021) 168–190.
- [4] Y. Zhu, C. Lv, Z. Yin, J. Ren, X. Yang, C.-L. Dong, H. Liu, R. Cai, Y.-C. Huang, W. Theis, S. Shen, D. Yang, A [001]-Oriented Hittorf's Phosphorus Nanorods/Polymeric Carbon Nitride Heterostructure for Boosting Wide-Spectrum-Responsive Photocatalytic Hydrogen Evolution from Pure Water, *Angew. Chem.* 132 (2) (2020) 878–883.
- [5] Y. Jiang, Z. Sun, C. Tang, Y. Zhou, L. Zeng, L. Huang, Enhancement of photocatalytic hydrogen evolution activity of porous oxygen doped g-C₃N₄ with nitrogen defects induced by changing electron transition, *Appl. Catal. B: Environ.* 240 (2019) 30–38.
- [6] Y. Wang, A. Vogel, M. Sachs, R.S. Sprick, L. Wilbraham, S.J.A. Moniz, R. Godin, M. A. Zwijnenburg, J.R. Durrant, A.I. Cooper, J. Tang, Current understanding and challenges of solar-driven hydrogen generation using polymeric photocatalysts, *Nature, Energy* 4 (9) (2019) 746–760.
- [7] Z. Sun, Y. Jiang, W.u. Wang, R. Zhong, Y. Pu, Q. Chen, B.o. Nan, J. He, L. Huang, Visible-light-stimulated alkalis-triggered platinum cocatalyst with electron deficient interface for hydrogen evolution, *ChemCatChem* 12 (8) (2020) 2189–2193.
- [8] B.o. Jiang, H. Huang, W. Gong, X. Gu, T. Liu, J. Zhang, W. Qin, H. Chen, Y. Jin, Z. Liang, L. Jiang, Wood-Inspired Binder Enabled Vertical 3D Printing of g-C₃N₄/CNT Arrays for Highly Efficient Photoelectrochemical Hydrogen Evolution, *Adv. Funct. Mater.* 31 (45) (2021) 2105045, <https://doi.org/10.1002/adfm.v31.45.1002/adfm.202105045>.
- [9] Y. Dai, C. Poidevin, C. Ochoa-Hernández, A.A. Auer, H. Tuysüz, A Supported Bismuth Halide Perovskite Photocatalyst for Selective Aliphatic and Aromatic C–H Bond Activation, *Angew. Chem. Int. Ed. Engl.* 59 (14) (2020) 5788–5796.
- [10] Y.-X. Tan, Z.-M. Chai, B.-H. Wang, S. Tian, X.-X. Deng, Z.-J. Bai, L. Chen, S. Shen, J.-K. Guo, M.-Q. Cai, C.-T. Au, S.-F. Yin, Boosted Photocatalytic Oxidation of Toluene into Benzaldehyde on CdIn₂S₄-CdS: Synergistic Effect of Compact Heterojunction and S-Vacancy, *ACS Catal.* 11 (5) (2021) 2492–2503.
- [11] K. Su, H. Liu, B. Zeng, Z. Zhang, N. Luo, Z. Huang, Z. Gao, F. Wang, Visible-Light-Driven Selective Oxidation of Toluene into Benzaldehyde over Nitrogen-Modified Nb₂O₅ Nanomeshes, *ACS Catal.* 10 (2) (2020) 1324–1333.
- [12] X. Wang, K. Maeda, A. Thomas, K. Takanabe, G. Xin, J.M. Carlsson, K. Domen, M. Antonietti, A metal-free polymeric photocatalyst for hydrogen production from water under visible light, *Nat. Mater.* 8 (2009) 76–80.
- [13] C. Zhao, Z. Chen, J. Xu, Q. Liu, H. Xu, H. Tang, G. Li, Y. Jiang, F. Qu, Z. Lin, X. Yang, Probing supramolecular assembly and charge carrier dynamics toward enhanced photocatalytic hydrogen evolution in 2D graphitic carbon nitride nanosheets, *Appl. Catal. B: Environ.* 256 (2019) 117867, <https://doi.org/10.1016/j.apcatb.2019.117867>.
- [14] J. Yi, T. Fei, L.i. Li, Q. Yu, S. Zhang, Y. Song, J. Lian, X. Zhu, J. Deng, H. Xu, H. Li, Large-scale production of ultrathin carbon nitride-based photocatalysts for high-yield hydrogen evolution, *Appl. Catal. B: Environ.* 281 (2021) 119475, <https://doi.org/10.1016/j.apcatb.2020.119475>.
- [15] Z. Zhou, Y. Zhang, Y. Shen, S. Liu, Y. Zhang, Molecular engineering of polymeric carbon nitride: advancing applications from photocatalysis to biosensing and more, *Chem. Soc. Rev.* 47 (7) (2018) 2298–2321.
- [16] Z. Chen, S. Zhang, Y. Liu, N.S. Alharbi, S.O. Rabah, S. Wang, X. Wang, Synthesis and fabrication of g-C₃N₄-based materials and their application in elimination of pollutants, *Sci. Total Environ.* 731 (2020), 139054.
- [17] C. Bie, B. Cheng, J. Fan, W. Ho, J. Yu, Enhanced solar-to-chemical energy conversion of graphitic carbon nitride by two-dimensional cocatalysts, *EnergyChem* 3 (2) (2021) 100051, <https://doi.org/10.1016/j.enchem.2021.100051>.
- [18] X. Xiao, Y. Gao, L. Zhang, J. Zhang, Q. Zhang, Q. Li, H. Bao, J. Zhou, S. Miao, N. Chen, A promoted charge separation/transfer system from Cu single atoms and C₃N₄ layers for efficient photocatalysis, *Adv. Mater.* 32 (2020) 2003082.
- [19] W. Jiang, Q. Ruan, J. Xie, X. Chen, Y. Zhu, J. Tang, Oxygen-doped Carbon Nitride Aerogel: A Self-supported Photocatalyst for Solar-to-chemical Energy Conversion, *Appl. Catal. B Environ.* 236 (2018) 428–435.
- [20] L. Luo, Z. Gong, J. Ma, K. Wang, H. Zhu, K. Li, L. Xiong, X. Guo, J. Tang, Ultrathin sulfur-doped holey carbon nitride nanosheets with superior photocatalytic hydrogen production from water, *Appl. Catal. B: Environ.* 284 (2021), 119742.
- [21] Y. Kang, Y. Yang, L.-C. Yin, X. Kang, L. Wang, G. Liu, H.-M. Cheng, Selective Breaking of Hydrogen Bonds of Layered Carbon Nitride for Visible Light Photocatalysis, *Adv. Mater.* 28 (30) (2016) 6471–6477.
- [22] M.Z. Rahman, P.C. Tapping, T.W. Kee, R. Smernik, N. Spooner, J. Moffatt, Y. Tang, K. Davey, S.-Z. Qiao, A Benchmark Quantum Yield for Water Photoreduction on Amorphous Carbon Nitride, *Adv. Funct. Mater.* 27 (39) (2017) 1702384, <https://doi.org/10.1002/adfm.v27.3910.1002/adfm.201702384>.
- [23] W.u. Wang, J. Cui, Z. Sun, L. Xie, X. Mu, L. Huang, J. He, Direct Atomic-Scale Structure and Electric Field Imaging of Triazine-Based Crystalline Carbon Nitride, *Adv. Mater.* 33 (48) (2021) 2106359, <https://doi.org/10.1002/adma.v33.4810.1002/adma.202106359>.
- [24] Z. Sun, W.u. Wang, Q. Chen, Y. Pu, H. He, W. Zhuang, J. He, L. Huang, A hierarchical carbon nitride tube with oxygen doping and carbon defects promotes solar-to-hydrogen conversion, *J. Mater. Chem. A* 8 (6) (2020) 3160–3167.
- [25] B. Tian, Y. Wu, G. Lu, Metal-free plasmonic boron phosphide/graphitic carbon nitride with core-shell structure photocatalysts for overall water splitting, *Appl. Catal. B: Environ.* 280 (2021) 119410, <https://doi.org/10.1016/j.apcatb.2020.119410>.
- [26] S. An, G. Zhang, K. Li, Z. Huang, X. Wang, Y. Guo, J. Hou, C. Song, X. Guo, Self-Supporting 3D Carbon Nitride with Tunable n-π* Electronic Transition for Enhanced Solar Hydrogen Production, *Adv. Mater.* 33 (49) (2021) 2104361, <https://doi.org/10.1002/adma.v33.4910.1002/adma.202104361>.
- [27] Y. Ma, F. Liu, Y. Liu, X. Lan, Y. Zhu, J. Shi, W. Jiang, G. Wang, S.H. Park, In-situ intramolecular synthesis of tubular carbon nitride S-scheme heterojunctions with exceptional in-plane exciton splitting and mechanism insight, *Chem. Eng. J.* 414 (2021), 128802.
- [28] Y. Jiang, Z. Sun, Q. Chen, C. Cao, Y. Zhao, W. Yang, L. Zeng, L. Huang, Fabrication of 0D/2D TiO₂ Nanodots/g-C₃N₄ S-scheme heterojunction photocatalyst for efficient photocatalytic overall water splitting, *Appl. Surf. Sci.* 571 (2021), 151287.
- [29] Y. Zhou, C. Zhang, D. Huang, W. Wang, Y. Zhai, Q. Liang, Y. Yang, S. Tian, H. Luo, D. Qin, Structure defined 2D Mo₂C/2D g-C₃N₄ Van der Waals heterojunction: Oriented charge flow in-plane and separation within the interface to collectively promote photocatalytic degradation of pharmaceutical and personal care products, *Appl. Catal. B: Environ.* 301 (2021), 120749.
- [30] P. Ma, X. Zhang, C. Wang, Z. Wang, K. Wang, Y. Feng, J. Wang, Y. Zhai, J. Deng, L. Wang, Band alignment of heterojunction by anchoring CN quantum dots on g-C₃N₄ (0D/2D) enhance photocatalytic hydrogen peroxide evolution, *Appl. Catal. B: Environ.* 300 (2021), 120736.
- [31] E.A. Dil, M. Ghaedi, A. Asfaram, F. Mehrabi, F. Sadeghfari, Efficient adsorption of Azure B onto CNTs/Zn: ZnO@Ni₂P-NCs from aqueous solution in the presence of ultrasound wave based on multivariate optimization, *J. Ind. Eng. Chem.* 74 (2019) 55–62.
- [32] E.A. Dil, M. Ghaedi, A. Asfaram, F. Mehrabi, A.A. Bazrafshan, L. Tayebi, Synthesis and application of Ce-doped TiO₂ nanoparticles loaded on activated carbon for ultrasound-assisted adsorption of Basic Red 46 dye, *Ultrason. Sonochem.* 58 (2019), 104702.
- [33] R. Bagheri, M. Ghaedi, A. Asfaram, E. Alipanahpour Dil, H. Javadian, RSM-CCD design of malachite green adsorption onto activated carbon with multimodal pore size distribution prepared from Amygdalus scoparia: Kinetic and isotherm studies, *Polyhedron* 171 (2019) 464–472.
- [34] E. Sharifpour, E. Alipanahpour Dil, A. Asfaram, M. Ghaedi, A. Goudarzi, Optimizing adsorptive removal of malachite green and methyl orange dyes from simulated wastewater by Mn-doped Cu₂O-Nanoparticles loaded on activated carbon using CCD-RSM: Mechanism, regeneration, isotherm, kinetic, and thermodynamic studies, *Appl. Organomet. Chem.* 33 (2019), e4768.
- [35] E.A. Dil, M. Ghaedi, G.R. Ghezelbash, A. Asfaram, A.M. Ghaedi, F. Mehrabi, Modeling and optimization of Hg²⁺ ion biosorption by live yeast *Yarrowia lipolytica* 70562 from aqueous solutions under artificial neural network-genetic algorithm and response surface methodology: kinetic and equilibrium study, *RSC adv.* 6 (2016) 54149–54161.
- [36] Y. Fang, Y. Xu, X. Li, Y. Ma, X. Wang, Coating polymeric carbon nitride photoanodes on conductive Y: ZnO nanorod arrays for overall water splitting, *Angew. Chem.* 130 (2018) 9897–9901.
- [37] Y. Zheng, L. Lin, X. Ye, F. Guo, X. Wang, Helical graphitic carbon nitrides with photocatalytic and optical activities, *Angew. Chem. Int. Ed. Engl.* 53 (2014) 11926–11930.
- [38] J. Liu, X.-T. Yan, X.-S. Qin, S.-J. Wu, H. Zhao, W.-B. Yu, L.-H. Chen, Y. Li, B.-L. Su, Light-assisted preparation of heterostructured g-C₃N₄/ZnO nanorods arrays for enhanced photocatalytic hydrogen performance, *Catal. Today* 355 (2020) 932–936.
- [39] Y.S. Jun, E.Z. Lee, X. Wang, W.H. Hong, G.D. Stucky, A. Thomas, From Melamine-Cyanuric Acid Supramolecular Aggregates to Carbon Nitride Hollow Spheres, *Adv. Funct. Mater.* 23 (2013) 3661–3667.
- [40] S. Guo, Z. Deng, M. Li, B. Jiang, C. Tian, Q. Pan, H. Fu, Phosphorus-Doped Carbon Nitride Tubes with a Layered Micro-nanostructure for Enhanced Visible-Light Photocatalytic Hydrogen Evolution, *Angew. Chem. Int. Ed. Engl.* 55 (2016) 1830–1834.
- [41] Y. Xiao, G. Tian, W. Li, Y. Xie, B. Jiang, C. Tian, D. Zhao, H. Fu, Molecule Self-Assembly Synthesis of Porous Few-Layer Carbon Nitride for Highly Efficient Photoredox Catalysis, *J. Am. Chem. Soc.* 141 (6) (2019) 2508–2515.
- [42] W.u. Wang, Z. Sun, J. Feng, J. Cui, L. Huang, J. He, Three-dimensional Insight on Formation and Light-harvesting of Hollow-structure Carbon Nitride, *ACS Appl. Energ. Mater.* 3 (7) (2020) 7020–7029.
- [43] Z. Luo, C. Li, S. Liu, T. Wang, J. Gong, Gradient doping of phosphorus in Fe₂O₃ nanoarray photoanodes for enhanced charge separation, *Chem. Sci.* 8 (1) (2017) 91–100.
- [44] Y. Zheng, L. Lin, B.o. Wang, X. Wang, Graphitic Carbon Nitride Polymers toward Sustainable Photoredox Catalysis, *Angew. Chem.* 54 (44) (2015) 12868–12884.
- [45] D.O. Scanlon, C.W. Dunnill, J. Buckeridge, S.A. Shevlin, A.J. Logsdail, S. M. Woodley, C.R.A. Catlow, M.J. Powell, R.G. Palgrave, I.P. Parkin, G.W. Watson,

- T.W. Keal, P. Sherwood, A. Walsh, A.A. Sokol, Band alignment of rutile and anatase TiO_2 , *Nat. Mater.* 12 (9) (2013) 798–801.
- [46] Y. Li, F. Gong, Q. Zhou, X. Feng, J. Fan, Q. Xiang, Crystalline isotype heptazine-/triazine-based carbon nitride heterojunctions for an improved hydrogen evolution, *Appl. Catal. B: Environ.* 268 (2020), 118381.
- [47] G. Zhang, L. Lin, G. Li, Y. Zhang, A. Savateev, S. Zafeiratos, X. Wang, M. Antonietti, Ionothermal Synthesis of Triazine-Heptazine-Based Copolymers with Apparent Quantum Yields of 60% at 420 nm for Solar Hydrogen Production from “Sea Water”, *Angew. Chem.* 130 (2018) 9516–9520.
- [48] X. Ruan, X. Cui, G. Jia, J. Wu, J. Zhao, D.J. Singh, Y. Liu, H. Zhang, L. Zhang, W. Zheng, Intramolecular heterostructured carbon nitride with heptazine-triazine for enhanced photocatalytic hydrogen evolution, *Chem. Eng. J.* 428 (2022), 132579.
- [49] H. Ou, P. Yang, L. Lin, M. Anpo, X. Wang, Carbon Nitride Aerogels for the Photoredox Conversion of Water, *Angew. Chem. Int. Ed. Engl.* 129 (2017) 10905–10910.
- [50] E. Wirnhier, M. Doblinger, D. Gunzelmann, J. Senker, B.V. Lotsch, W. Schnick, Poly(triazine imide) with intercalation of lithium and chloride ions [$(\text{C}_3\text{N}_3)_2(\text{NH}_{(x)}\text{Li}_{(1-x)})_3\text{LiCl}$]: a crystalline 2D carbon nitride network, *Chem. Eur. J.* 17 (2011) 3213–3221.
- [51] S. Trasatti, S. Trasatti, The absolute electrode potential: an explanatory note (Recommendations 1986), *Pure Appl. Chem.*, 58 (2009) 955–966.
- [52] Z. Sun, Y. Tan, J. Wan, L. Huang, In-depth understanding of the effects of intramolecular charge transfer on carbon nitride based photocatalysts, *Chin. J. Chem.* 39 (2021) 2044–2053.
- [53] Z. Sun, Y. Jiang, L. Zeng, X. Zhang, S. Hu, L. Huang, Controllable local electronic migration induced charge separation and red-shift emission in carbon nitride for enhanced photocatalysis and potential phototherapy, *Chem. Commun.* 55 (2019) 6002–6005.
- [54] Z. Sun, Y. Jiang, L. Zeng, L. Huang, Intramolecular Charge Transfer and Extended Conjugate Effects in Donor- π -Acceptor-Type Mesoporous Carbon Nitride for Photocatalytic Hydrogen Evolution, *ChemSusChem* 12 (2019) 1325–1333.
- [55] Z. Liu, J. Zhang, Y. Wan, J. Chen, Y. Zhou, J. Zhang, G. Wang, R. Wang, Donor-Acceptor structural polymeric carbon nitride with in-plane electric field accelerating charge separation for efficient photocatalytic hydrogen evolution, *Chem. Eng. J.* 430 (2022), 132725.